A Semantic-Aware and Multi-Guided Network for Infrared-Visible Image Fusion

Xiaoli Zhang, Liying Wang, Libo Zhao, Xiongfei Li, Siwei Ma, *Fellow, IEEE*

Abstract—Multi-modality image fusion aims at fusing modality-specific (complementarity) and modality-shared (correlation) information from multiple source images. To tackle the problem of the neglect of inter-modal information, high-frequency information loss and limited attention to downstream tasks, this paper focuses on how to model correlation-driven decomposing features and reason high-level graph representation by efficiently extracting complementary features and aggregating multi-guided features. We propose a three-branch encoder-decoder architecture along with corresponding fusion layers as the fusion strategy. The transformer with Multi-Dconv Head Transposed Attention and Local-enhanced Feed Forward network is used to extract shallow features after the depthwise convolution. In the three parallel branches of the encoder, Cross Attention and Invertible Block (CAI) enables to extract local features and preserve high-frequency texture details. Base Feature Extraction Module (BFE) with residual connections can capture long-range dependencies and enhance modality-shared information. Graph Reasoning Module (GR) is introduced to reason high-level cross-modality relations and simultaneously extract low-level detail features as CAI's modality-specific complementary information. Experiments demonstrate that our method obtains competitive results compared with state-of-the-art methods in visible/infrared image fusion and medical image fusion tasks. Moreover, we surpass other fusion methods in terms of subsequent tasks, averagely scoring 8.27% mAP@0.5 higher in object detection and 5.85% mIoU higher in semantic segmentation.

Index Terms—Image Fusion, Auto-encoder, Graph Neural Network, Cross Attention, Feature Aggregation.

I. Introduction

MULTI-MODAL image fusion has attracted widespread attention because it solves the limitation of single-modality imaging representation. For instance, in the realm of infrared and visible fusion [1]–[3], infrared imaging excels in highlighting thermal targets, particularly in challenging environmental conditions, albeit at the expense of resolution. Conversely, visible imaging is adept at preserving intricate texture details but is susceptible to variations in illumination conditions. Consequently, the effective integration of these two modal images enables their respective strengths to be leveraged, such as enhanced visual perception and the identification of salient objects. Fused images exhibit improved adaptability to complex scenarios, particularly when deployed

Corresponding author: Siwei Ma (swma@pku.edu.cn).

Xiaoli Zhang, Liying Wang, Libo Zhao, Xiongfei Li are with the Key Laboratory of Symbolic Computation and Knowledge Engineering of Ministry of Education, Jilin University, Changchun 130012, China.

Siwei Ma is with the Institute of Digital Media, School of Electronic Engineering and Computer Science, Peking University, Beijing 100871, China.

in downstream tasks such as object detection [4] and semantic segmentation [5], [6]. Moreover, image fusion finds extensive applications and extends to various computer vision tasks,
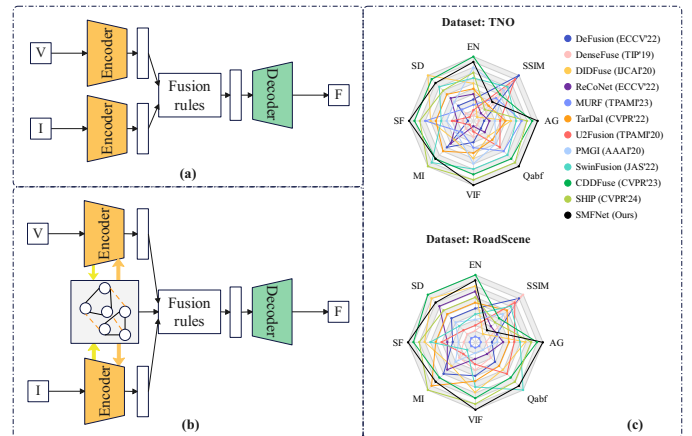

Fig. 1. (a) Pipeline of typical Auto-Encoder-based methods, consisting of encoders, a decoder and auxiliary fusion strategies; (b) Our proposed semantic-aware and multi-guided network; (c) We show the qualitative results of fused images on TNO and RoadScene datasets compared with eleven state-of-the-art methods via the radar plots.

including but not limited to medical image segmentation [7]–[9] and remote sensing [10].

In recent years, deep learning methods have become increasingly prevalent in the image fusion field. When dealing with multi-modal images, the primary challenge lies in extracting complementary features from diverse imaging sensors and integrating them into a single image. There are three mainstream methods in multi-modal image fusion: generative methods [11], [12], [13], [14], [15], unified frameworks [16], [17], [18], [19], [20] and auto-encoder methods [21], [22], [23], [24], [25], [26]. Some of these methods have achieved satisfactory performance when tackling specific image fusion tasks. **However, existing methods still face three challenges: (i)** Most methods do not fully consider the relationships between the two modal images during the image fusion training process; **(ii)** Local features extracted by convolutional neural networks (CNN) are difficult to control and easy to lose in the forward process, especially high-frequency information; and **(iii)** Most existing methods often overlook the facilitation of downstream tasks by the generated fused images, resulting in a lack of semantic information and salient targets. Consequently, their performance in downstream tasks is often unsatisfactory.

To tackle the aforementioned challenges, we propose a **S**emantic-Aware and **M**ulti-Guided Network for Infrared-Visible Image **F**usion **(SMFNet)**. **For challenge (i)**, we intro-

duce a Graph Reasoning module to model and reason about high-level relations between two modalities and extract low-level detail features. **For challenge (ii)**, a Cross Attention and Invertible Block (CAI) is employed to address information loss during the decomposing process to extract high-frequency features. Additionally, a base feature extraction module equipped with Multi-Dconv Head Transposed Attention (MDTA) and Local-enhanced Feed Forward (LeFF) network is proposed to capture global features with long-range dependencies. **For challenge (iii)**, we devise two novel loss functions for the two training stages. The loss function in the first stage guides the network to generate an image that closely resembles the two source images. The second loss function, utilized in the second stage, emphasizes the preservation of target intensity and semantic textures in the fused images, with the aim of benefiting downstream tasks. Our motivations, workflow of SMFNet and quantitative results on two datasets are illustrated in Fig. 1. In this paper, our contributions are as follows:

- We propose a **S**emantic-aware and **M**ulti-guided **Net**work for infrared-visible image **F**usion (SMFNet) with two training stages to fully decompose features and generate fused images by fusion strategy. Graph Reason Module is used to reason high-level cross-modality relations, and also extracts respective low-level detail features.
- The Cross Attention and Invertible Block is proposed to extract high-frequency detail features and preserve important information efficiently via learning an inverse process implicitly. The base Feature Extraction Module is applied to model long-range dependencies and obtain powerful global base features.
- A novel loss function based on the Gram matrix is introduced to better utilize semantic details of intensity targets to reconstruct source images. Correlation-driven decomposition loss is proposed to trade off modality-specific, modality-shared and graph-interaction features.
- Experiments show the SMFNet has satisfactory visual performance when compared with eleven state-of-the-art methods on TNO, $RoadScene$, $MSRS$, MIF datasets and in two major machine perception tasks, object detection and semantic segmentation.

The remainder of this paper is organized as follows. Related works and technologies are described in Section II. Section III demonstrates the semantic-aware and multi-guided network (SMFNet), including encoder, decoder, fusion strategy and loss function. Details about the experiments and evaluation are in Section IV. And Section V is the brief summary of the work.

II. RELATED WORKS

In this section, we review the existing infrared-visible image fusion algorithms in Section II-A. Then, some advanced methods of Transformer and Graph Neural Networks are illustrated in Sections II-B and II-C.

A. Infrared-Visible Image Fusion

Traditional approaches have been explored for infrared-visible image fusion in recent years. Multi-scale transform [27], [28], sparse representation-based [29], edge-preserving filter [30], and saliency-based methods [31] are widely recognized as representative methods. Besides, Zhao *et al.* [32] casted image fusion into a regression problem, seeking the solution in the hierarchical Bayesian manner inferred by expectation-maximization (EM) algorithm. These works have displayed stable performance and have been put into real-world applications. Unavoidably, traditional methods need hand-craft fusion rules and lead to generate artifacts surrounding the edge regions and halos surrounding the objects. The above issues have restricted further development faced with numerous application scenarios.

With the progress of deep-learning technologies, researchers focus on generative methods, unified frameworks and auto-encoder methods in order to explore a series of innovative ways to generate fused images for human vision and machine decision. In generative methods, Ma *et al.* [12] trained the generator to generate fused images and the discriminator to force fused images similar to the source images. The denoising diffusion probabilistic model (DDPM) [33] was introduced into image fusion with the aim of alleviating the unstable training and lack of interpretability for GAN-based methods. In unified frameworks, Xu *et al.* [16] proposed the incorporation of elastic weight consolidation into the loss function to enable the model to handle multi-fusion tasks effectively. Zhang *et al.* [18] offered an alternative approach by uniformly modeling image fusion tasks as the problem of maintaining texture and intensity proportions across source images. Evolved from traditional transforms [34], [35], in auto-encoder methods, Zhao *et al.* [25], [26] emphasized the encoder's role in decomposing the image into detailed features and background, with the decoder recovering the original image. Liang *et al.* [36] devised a pretext task in a self-supervised manner based on common and unique decomposition (CUD). Furthermore, in cooperative training methods, ReCoNet [37] simultaneously learns networks for fusion and registration, aiming to produce robust images for misaligned source images. Liu *et al.* [38] integrated differentiable neural architecture search (NAS) [39] with bi-level optimization into the training process to suit specific scenario applications. Zhao *et al.* [40] presents meta-learning as another avenue for joint training, generating features based on the designed network's capabilities. In MURF [41], image registration and fusion mutually reinforce each other, contributing to enhanced fusion outcomes. Recently, Zheng *et al.* [42] proposed a new paradigm based on synergistic high-order interaction in both channel and spatial dimensions.

B. Transformer in Image Processing

In 2020, Dosovitskiy *et al.* [43] proposed the Vision Transformer (ViT), which represents images as sequences of tokens, similar to how words are represented in natural language processing tasks. It has sparked significant interest and research in the application of Transformer-based architectures to computer vision (CV). Recently, subsequent works [44]–[51] have been proposed and applied in various CV tasks, such as image classification, high-resolution image restoration, image
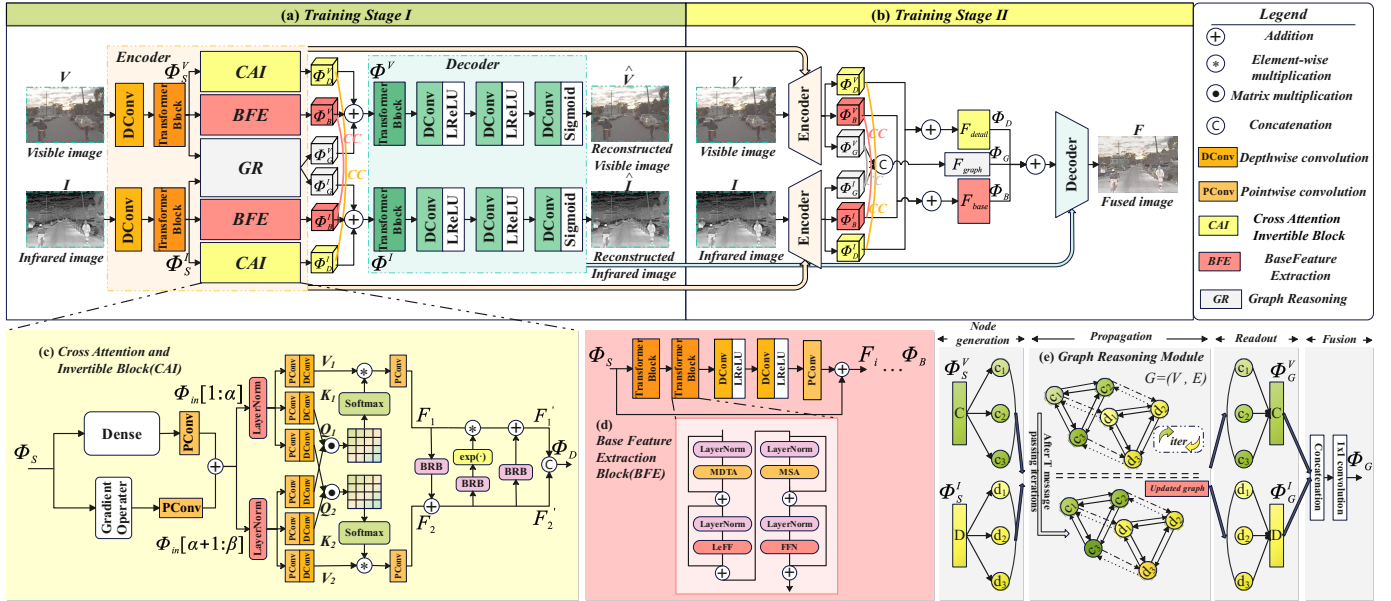
Fig. 2. The architecture of proposed SMFNet. (a) In training stage I, the reconstructed original images are obtained from a three-branch encoder and a decoder framework. Features extracted from CAI, BFE and GR are aggregated and then fed into the decoder. (b) In training stage II, modality-specific, modality-shared and graph low-level features are further fused by the proposed fusion strategy. Then decoder generates the fused image. (c) CAI shows the process of refining fine-grained features and retaining high-frequency information using cross-attention mechanism and invertible module. (d) BFE enhances long-range dependencies via residual connections. (e) GR based on GNN can model the high-level relationships between two modalities shallow features and reason low-level detail features simultaneously.

super-resolution, deraining and denoising. *SegFormer* [5] comprising a hierarchical Transformer encoder without positional encoding and lightweight MLP decoders, achieved efficient segmentation on Transformers. *SwinIR* [44], a strong baseline for image restoration, was equipped with several residual Swin Transformer blocks together with the residual connection as the deep feature extraction module. Wang *et al.* [45] proposed a non-overlapping window-based self-attention and added a depth-wise convolution layer into the feed-forward network to capture local context. Considering the translation invariance and the vital role of local relationships, Xiao *et al.* [46] proposed the stochastic window strategy to replace fixed local window strategy, which enjoys powerful representation. *XCiT* [47] proposed cross-covariance attention, a transposed version of self-attention mechanism, what's more, the interactions between keys and queries are based on cross-covariance matrix. Restormer [51] focusing on more informative features reduced the time and memory of key-query dot-product interaction in self-attention layers.

C. Graph Neural Networks

As a typical deep-learning network, Graph Neural Networks (GNN) [52] can model complex links among interpersonal relationships in social networks , thus it has been widely applied in the realm of recommender systems [53]. The Graph Convolutional Networks (GCN) [54] were first proposed for semi-supervised learning on graph-structured data. As for computer vision, Wang *et al.* [55] answered the question: how do humans recognize the action "opening a book", with the definition of graph nodes by the object region from different frames in the video. Exploring the higher perfor-

mance of semantic segmentation, object detection and instance segmentation tasks, Li *et al.* [56] proposed to transform a two-dimensional image into a graph structure. The graph's vertices define clusters of pixels and the edges define the similarity between these regions in a feature space. Han *et al.* [57] proposed Vision GNN (ViG), viewing image patches as nodes, which introduced graph convolution for aggregating and updating graph information and FFN layers for node feature transformation. To go a step further, *Vision HGNN* [58] proposed that an image is more than a graph of nodes. They transcended conventional linkages and introduced the concept of hypergraph to encapsulate image information, which is a more universal structure. Recently, Xu *et al.* [59] proposed a dual-space graph-based interaction network for real-time scene comprehension, which exploited cross-graph and inner-graph relations and extracted contextual information. In RGB-D salient object detection [60], [61], researchers aim at addressing a major technical challenge: how to fully leverage cross-modal complementary features. Correspondingly, GNNs have shown their abilities to learn high-level relations and describe low-level details simultaneously [62].

III. PROPOSED METHOD

In this section, the workflow of the proposed SMFNet is described in Section III-A. Then, the main structure of the encoder is in Section III-B. Furthermore, the proposed decoder and fusion strategy can be found in Sections III-C and III-D. Finally, The loss function is discussed in Section III-E.

A. Overview

As illustrated in Fig. 2, the proposed SMFNet is constructed using an encoder-decoder architecture. To compre-

hensively extract features, we have meticulously designed an encoder with three branches. Through the encoder, we extract shallow features and subsequently obtain various types of deep features, including local high-frequency information and background low-frequency information. There are three main parallel modules: Cross Attention and Invertible (CAI) block, Base Feature Extraction (BFE) module, and Graph Reasoning (GR) module. Following the aggregation of modality-specific features and modality-shared features from three branches, the decoder reconstructs the original image.

Overall, **in training stage I**, the encoder's capability to extract features from the source image and the decoder's ability to obtain the reconstructed image are trained in an iterative procedure via pursuing minimal reconstruction loss; **In training stage II**, fusion layers, consistent with the encoding branches, are proposed as the fusion strategy. Constraining the similarity between the source images and the fused image in terms of structure, texture details and intensity, SMFNet can generate an image that benefits visual and computer perception; **In the inference phase**, the network structure utilized during training stage II can be directly applied to validate the efficacy of image fusion and assess the model's generalization capability in practical applications.

B. Encoder

1) Shallow Feature Extraction: In this part, we mainly extract shallow features

$$\mathbf{\Phi}_S^V = SFE(\mathbf{V}), \mathbf{\Phi}_S^I = SFE(\mathbf{I}). \tag{1}$$

where $\mathbf{I} \in \mathbb{R}^{H \times W \times 1}$ and $\mathbf{V} \in \mathbb{R}^{H \times W \times 3}$ denote the infrared and visible images, respectively. SFE represents the shallow feature extraction module, comprising a depthwise 3×3 convolution and a transformer with multi-head self-attention.

2) Cross Attention and Invertible (CAI) block: The CAI extracts high frequency information from shallow features

$$\mathbf{\Phi}_D^V = CAI(\mathbf{\Phi}_S^V), \mathbf{\Phi}_D^I = CAI(\mathbf{\Phi}_S^I). \tag{2}$$

The main structure of CAI is shown in Fig. 2 (c). **Firstly**, to extract fine-grained detail information, we introduce a gradient and residual dense block benefiting from the Sobel operator. The block can be represented as

$$\mathbf{\Phi}_{in} = PConv(Dense((\mathbf{\Phi}_S)) + PConv(\nabla(\mathbf{\Phi}_S)), \tag{3}$$

where $\mathbf{\Phi}_S$ indicates infrared/visible shallow features extracted by SFE, ∇ denotes the sobel gradient operator. As the variant of resblock, dense connection makes full use of features extracted from convolutions and activate functions. Gradient magnitude is calculated to remove channel dimension differences.

Secondly, to aggregate the information from CNN's dual branches through interactive cross-attention mechanism and information invertibility, we propose a cross-attention module with the ability of local feature extraction. We set $\mathbf{\Phi}_{in}[1:\alpha]$ and $\mathbf{\Phi}_{in}[\alpha+1:\beta]$ separated from $\mathbf{\Phi}_{in}[1:\beta]$ as intermediate features used for the dual-branch block. $\mathbf{Q}_1, \mathbf{Q}_2 \in \mathbb{R}^{H \times W \times C}$, $\mathbf{K}_1, \mathbf{K}_2 \in \mathbb{R}^{C \times H \times W}$, $\mathbf{V}_1, \mathbf{V}_2 \in \mathbb{R}^{H \times W \times C}$. $\{\mathbf{Q}_1, \mathbf{K}_1, \mathbf{V}_1\}$ and $\{\mathbf{Q}_2, \mathbf{K}_2, \mathbf{V}_2\}$ are obtained after $\mathbf{\Phi}_{in}[1:\alpha]$ and $\mathbf{\Phi}_{in}[\alpha+$

$1:\beta]$ pass through the layer norm, pointwise convolution and depthwise convolution, respectively. The cross-attention module can be represented as

$$\mathbf{F}_1 = \mathbf{V}_1 * Softmax(\mathbf{K}_1, \mathbf{Q}_2/T), \tag{4}$$

$$\mathbf{F}_2 = \mathbf{V}_2 * Softmax(\mathbf{K}_2, \mathbf{Q}_1/T). \tag{5}$$

where T means temperature, a learnable scaling parameter. The cross-attention module can divide the number of channels to the head, which achieves two branches of learning attention maps simultaneously.

Finally, to refine the feature extracted from the above cross-attention module, and efficiently obtain semantic feature as expected, we learn an inverse process implicitly [63]–[66]. The intermediate features are formulated as

$$\mathbf{F}_1' = \mathbf{F}_1 \otimes exp(\psi(\mathbf{F}_2)) + \psi(\mathbf{F}_2), \tag{6}$$

$$\mathbf{F}_2' = \mathbf{F}_2 + \psi(\mathbf{F}_1), \tag{7}$$

where $\otimes$ denotes the element-wise multiplication, $\psi(\cdot)$ refers to the Bottleneck Residual Block (BRB), and the $exp(\cdot)$ indicates the exponential function. The output of CAI $\mathbf{\Phi}_D$ can be obtained by the concatenation of $\mathbf{F}_1'$ and $\mathbf{F}_2'$.

3) Base Feature Extraction (BFE) Module: Contrary to CAI, the BFE extracts low-frequency global features from SFE-extracted shallow features

$$\mathbf{\Phi}_B^V = BFE(\mathbf{\Phi}_S^V), \mathbf{\Phi}_B^I = BFE(\mathbf{\Phi}_S^I). \tag{8}$$

The main structure of BFE is in Fig. 2 (d). Using Multi-Dconv Head Transposed Attention (MDTA), the transformer implements channel-dimension self-attention rather than the spatial dimension. It computes the cross-covariance among channels to generate an attention map to model global features with linear complexity. Local-enhanced Feed Forward (LeFF) Network, adding depth-wise convolution to Feed Forward Network (FFN) aims to reduce limited capability of leveraging local context. BFE can be defined as follows in detail

$$\mathbf{F}_0 = \mathbf{\Phi}_S, \tag{9}$$

$$\mathbf{F}_1 = Conv(\rho(\rho(\mathbf{F}_0))) + \mathbf{F}_0, \tag{10}$$

$$\mathbf{\Phi}_B = Conv(\rho(\rho(\mathbf{F}_1))) + \mathbf{F}_1, \tag{11}$$

where $\rho(\cdot)$ is the residual BFE block. The residual connection promotes feature aggregation from different feature levels during the phase of establishing long-range dependencies.

4) Graph Reasoning (GR) Module: The GR module is the third branch in the encoder, and it can be represented as

$$\mathbf{\Phi}_G^V = GR(\mathbf{\Phi}_S^V), \mathbf{\Phi}_G^I = GR(\mathbf{\Phi}_S^I). \tag{12}$$

As shown in Fig. 2 (e), the GR module is composed of node embedding, edge embedding, information delivery and node update, aiming at hierarchically reason about relations between two modalities and exploring useful information.

Graph Creation. We set $\mathbf{C} = [c_1, c_2, ..., c_n]$ and $\mathbf{D} = [d_1, d_2, ..., d_n]$ as nodes from visible and infrared, two kinds of modalities with n scales. $\mathbf{G} = (\mathbf{V}, \mathbf{E})$ stands for a directed graph. The inner nodes $V = \mathbf{C} \cup \mathbf{D}$. When starting a graph,
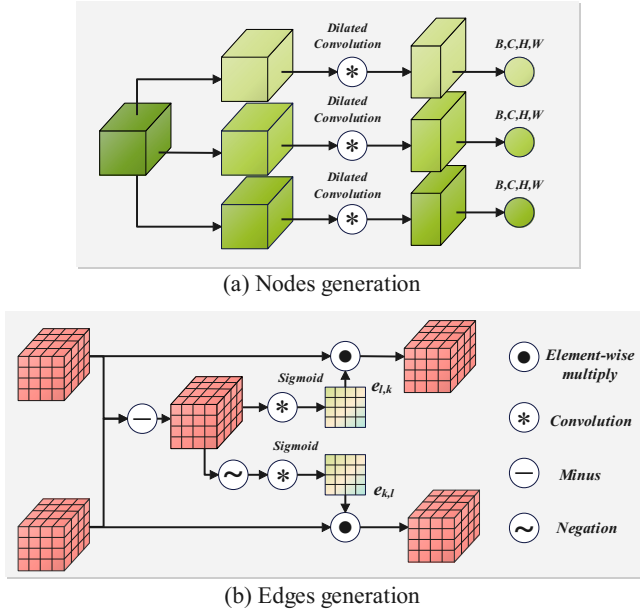
(a) Nodes generation

(b) Edges generation

Fig. 3. Specific illustration for nodes and edges generating process in graph reasoning module.

$c_i \leftrightarrow c_j$ and $d_i \leftrightarrow d_j$ belong to the same modality but different scales, $c_i \leftrightarrow d_i$ are the same scale but different modalities meanwhile. $N = 2 \cdot n$ and $N(l)$ stands for the number of nodes totally in graph G. The generation process of nodes and edges is illustrated in Fig. 3 (a) and (b).

Multi-scale Nodes Embedding. Each scale node has the shape $c_i^{(0)}$, $d_i^{(0)} \in \mathbb{R}^{H \times W \times C}$. For example, for the current nodes $c_i \in \mathbf{C}$ generation

$$\mathbf{c}_i^{(0)} = Conv(Pool(c_i^{(0)})), \tag{13}$$

where $Pool(\cdot)$ implements triple branches pooling and convolution operations.

Edges Embedding. Assume that $v_k, v_l \in V$, including nodes from visible/infrared modalities c_i and d_i, therefore, we obtain directed edges generation scheme from v_k to v_l

$$e_{k,l} = Conv(v_l - v_k). \tag{14}$$

Information delivery. After nodes and edges generation, information is transferred from the last node to the current one via powerful edges. We set $m_{k,l}^{(t)}$ as message from v_k to v_l via $e_{k,l}$ in $t-1$ state while delivering

$$m_{k,l}^{(t)} = \sum_{k \in N(l)} Sigmoid(e_{k,l}^{(t-1)}) \cdot v_k^{(t-1)}. \tag{15}$$

Nodes Update. Next to the message delivery, GR module learns intricate cross-modality relations, and nodes are updated through a GRU mechanism so that we obtain the updated node as $v^{(t)}$

$$v_l^{(t)} = \sum_{k \in N(l)} F_{GRU}(v_l^{(t-1)}, m_{k,l}^{(t-1)}). \tag{16}$$

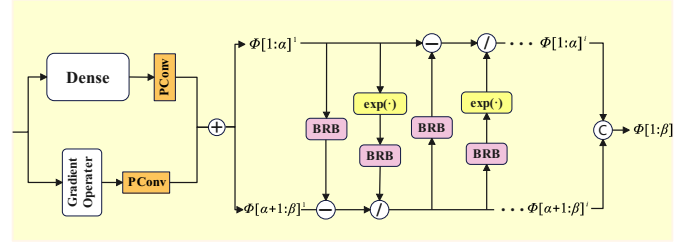Then, C and D can be merged separately through the convolution operation.

Fig. 4. Proposed detail fusion layers in training stage II.

C. Fusion Strategy

The functions of F_{detail}, F_{base}, F_{graph} are fusion layers to fuse detail, base and graph reasoning features, respectively.

$$\mathbf{\Phi}_D = F_{detail}(\mathbf{\Phi}_D^V, \mathbf{\Phi}_D^I), \mathbf{\Phi}_B = F_{base}(\mathbf{\Phi}_B^V, \mathbf{\Phi}_B^I), \tag{17}$$

$$\mathbf{\Phi}_G = F_{graph}(\mathbf{\Phi}_G^V, \mathbf{\Phi}_G^I). \tag{18}$$

Detail fusion layers are shown in Fig. 4. We set $Output(\cdot)$ as the output of the one branch. Mathematical expressions are as follows:

$$Output(\mathbf{\Phi}[1:\alpha]^{i+1}) = (\mathbf{\Phi}[1:\alpha]^i - \psi(\mathbf{\Phi} \\ [\alpha+1:\beta]^i)) \otimes exp(-\alpha(\psi(\mathbf{\Phi}[\alpha+1:\beta]^i))), \tag{19}$$

$$Output(\mathbf{\Phi}[\alpha+1:\beta]^{i+1}) = (\mathbf{\Phi}[\alpha+1:\beta]^i - \\ \psi(\mathbf{\Phi}[1:\alpha]^i)) \otimes exp(-\alpha(\psi(\mathbf{\Phi}[1:\alpha]^i))). \tag{20}$$

The ith layer designed for fusing cross-modality detail feature is shown as Eqs. (19) and (20). Eventually, the last two layers' features are concatenated into the decoder part. As described in Fig. 2 (e), $\mathbf{\Phi}_V^G$, $\mathbf{\Phi}_I^G$ from visible and infrared modalities are concatenated into a pointwise 1×1 convolution to fuse the output of read out part.

In consistency with the base feature extraction structure in the encoder, the base fusion layer is composed of a transformer the same as the block in SFE with MDTA and LeFF aiming at fusing global features $\mathbf{\Phi}_B^V$ and $\mathbf{\Phi}_B^I$.

D. Decoder

The decomposed features are aggregated together into a decoder to output original images (in stage I) or fused images (in stage II).

In stage I, the outputs of the decoder, reconstructed original images are

$$\hat{\mathbf{I}} = D(\mathbf{\Phi}_D^I, \mathbf{\Phi}_B^I, \mathbf{\Phi}_G^I), \hat{\mathbf{V}} = D(\mathbf{\Phi}_D^V, \mathbf{\Phi}_B^V, \mathbf{\Phi}_G^V). \tag{21}$$

In stage II, the output of the decoder, fused image is

$$\mathbf{F} = D(\mathbf{\Phi}_D, \mathbf{\Phi}_B, \mathbf{\Phi}_G). \tag{22}$$

The transformer block within the decoder adopts an identical structure to those in the SFE and the base fusion layer. It utilizes depthwise convolution to reconstruct aggregated features from the space $\mathbb{R}^{B \times C \times H \times W}$ to $\mathbb{R}^{H \times W \times 1}$.

E. Loss Function

In stage I, we train a reconstruction network with two-fold objectives: it should output reconstructed images without any loss of visual detail and also decompose the input images into base and detail layers. Therefore, the total loss is formulated as

$$\mathcal{L}_{total}^I = \underbrace{\mathcal{L}_{vi} + \mathcal{L}_{ir}}_{Reconstruction\ loss} + \alpha_1 \underbrace{\mathcal{L}_{decomp}^I}_{Decomposition\ loss}, \quad (23)$$

where $\mathcal{L}_{vi}$ and $\mathcal{L}_{ir}$ are the reconstruction losses for visible and infrared images, respectively. $\mathcal{L}_{decomp}^I$ denotes the feature decomposition loss. α_1 is a balancing factor. Both the two reconstruction losses $\mathcal{L}_{vi}$ and $\mathcal{L}_{ir}$ have structural loss $\mathcal{L}_{SSIM}$ and gradient loss $\mathcal{L}_{grad}$. $\mathcal{L}_{vi}$ is defined as

$$\mathcal{L}_{vi} = \beta_1 \mathcal{L}_{SSIM}(\mathbf{V}, \hat{\mathbf{V}}) + \beta_2 \mathcal{L}_{grad}(\mathbf{V}, \hat{\mathbf{V}}), \quad (24)$$

where the gradient loss is defined as $\mathcal{L}_{grad}(\mathbf{V}, \hat{\mathbf{V}}) = || |\nabla V| - |\nabla \hat{V}| ||_1$ (∇ denotes the gradient operator), and the structural loss is defined as $\mathcal{L}_{SSIM}(\mathbf{V}, \hat{\mathbf{V}}) = 1 - SSIM(\mathbf{V}, \hat{\mathbf{V}})$. $SSIM$ is the structural similarity index, which measures the similarity of two images in terms of luminance, contrast, and structure [67].

In Eq. (23), the reconstruction loss for the infrared image is defined as

$$\mathcal{L}_{ir} = \mathcal{L}_{semantic}(\mathbf{I}, \hat{\mathbf{I}}) + \beta_1 \mathcal{L}_{SSIM}(\mathbf{I}, \hat{\mathbf{I}}) + \beta_2 \mathcal{L}_{grad}(\mathbf{I}, \hat{\mathbf{I}}), \quad (25)$$

where $\mathcal{L}_{grad}(I, \hat{I})$ and $\mathcal{L}_{SSIM}(I, \hat{I})$ in $\mathcal{L}_{ir}$ can be obtained in the same way as the ones in $\mathcal{L}_{vi}$, and β_1, β_2 are set the same as Eq. (24). As infrared images contain minimal detailed information about the background but offer a clear display of object shapes and contours, the reconstructed infrared images should retain the crucial and salient information of the original images. Therefore, we define the $\mathcal{L}_{semantic}$ as

$$\mathcal{L}_{semantic}(\mathbf{I}, \hat{\mathbf{I}}) = ||\mathbf{Gr}(\mathbf{I}), \mathbf{Gr}(\hat{\mathbf{I}})||_2, \quad (26)$$

where $\mathbf{Gr}(\cdot)$ represents Gram matrix. The reason why the matrix is employed is that it contains the semantic features of images [68].

According to decomposed features from the encoder, we assume that modality-specific information has a lower value of correlation coefficient and modality-shared information has a higher correlation value. $\mathcal{L}_{decomp}^I$ is formulated as

$$\mathcal{L}_{decomp}^I = \frac{(CC(\Phi_D^{\mathbf{V}}, \Phi_D^I))^2}{CC(\Phi_B^V, \Phi_B^I) + \delta}, \quad (27)$$

where $CC(\cdot)$ denotes the correlation coefficient. δ is set to 1.01, which can guarantee gradient descent and optimization.

In stage II, the total loss is

$$\mathcal{L}_{total}^{II} = \mathcal{L}_{intensity}^{II} + \alpha_2 \mathcal{L}_{decomp}^{II} + \alpha_3 \mathcal{L}_{grad}^{II}, \quad (28)$$

where $\mathcal{L}_{intensity}^{II}$ and $\mathcal{L}_{grad}^{II}$ are inspired by [69], building the restriction among the fused image $\mathbf{F}$ and the two source images $\mathbf{V}$ and $\mathbf{I}$ by

$$\mathcal{L}_{intensity}^{II} = ||\mathbf{F} - \max(|\mathbf{I}|, |\mathbf{V}|)||_1, \quad (29)$$

$$\mathcal{L}_{grad}^{II} = || |\nabla \mathbf{F}| - \max(|\nabla \mathbf{I}|, |\nabla \mathbf{V}|)||_1. \quad (30)$$

Different from $\mathcal{L}_{decomp}^I$, high-frequency information shows more texture and details, whereas low-frequency information emphasizes background and base features. $CC(\Phi_G^V, \Phi_G^I)$ is added to balance features extracted from other branches and also as the complementary for simple modality-specific features

$$\mathcal{L}_{decomp}^{II} = \frac{(CC(\Phi_D^V, \Phi_D^I))^2 + (CC(\Phi_G^V, \Phi_G^I))^2}{CC(\Phi_B^V, \Phi_B^I) + \delta}. \quad (31)$$

IV. EXPERIMENTS

In this section, datasets and experimental settings are first described in Sections IV-A and IV-B. Subsequently, we conduct experiments to justify the superiority of the proposed algorithm by answering the following six questions:

- **RQ1**: How does the proposed method perform on the mainstream infrared-visible image fusion datasets?
- **RQ2**: Whether the proposed method generates task-oriented fused images to facilitate downstream tasks compared to other SOTA fusion algorithms?
- **RQ3**: How does the proposed model perform on other types of image fusion?
- **RQ4**: How do the proposed structures in the encoding network and fusion strategy influence the performance of the proposed model?
- **RQ5**: What role does the loss function proposed in this article play in guiding the neural network training process?
- **RQ6**: Why do we have two training stages?

A. Experiment Configuration

In the experimental setup, we partitioned the dataset into three distinct subsets for training, validation, and testing purposes. Specifically, we employed 1083 image pairs from [70] for training, while 50 RoadScene pairs served as the validation set. For testing, we utilized a combination of datasets, including 25 pairs from TNO [71], 50 pairs from RoadScene [16], and 361 pairs from MSRS (Multi-Spectral Road Scenarios) [70]. Although our model supports inputs of arbitrary size, we ensure that each iteration receives the same amount of data. During the training phase, the MSRS images were initially converted into grayscale and then cropped into patches of dimensions 128×128. The training process encompassed a total of 120 epochs, with the initial 40 epochs designated as the first training stage, followed by an additional 80 epochs constituting the second stage. The batch size was fixed at 6 throughout the training procedure.

As for hyperparameters in Eqs. (23), (24), (25) and (28), α_1 was uniformly set to 5; β_1 and β_2 were uniformly set to 8 and 10 in training stage I; α_2 and α_3 were set to 10 and 2 in training stage II. We used the Adam optimizer, and the initial learning rate was $1e^{-4}$ without weight decay. Experiments were executed on a PC with two NVIDIA GeForce 4090 GPUs and the pytorch framework.
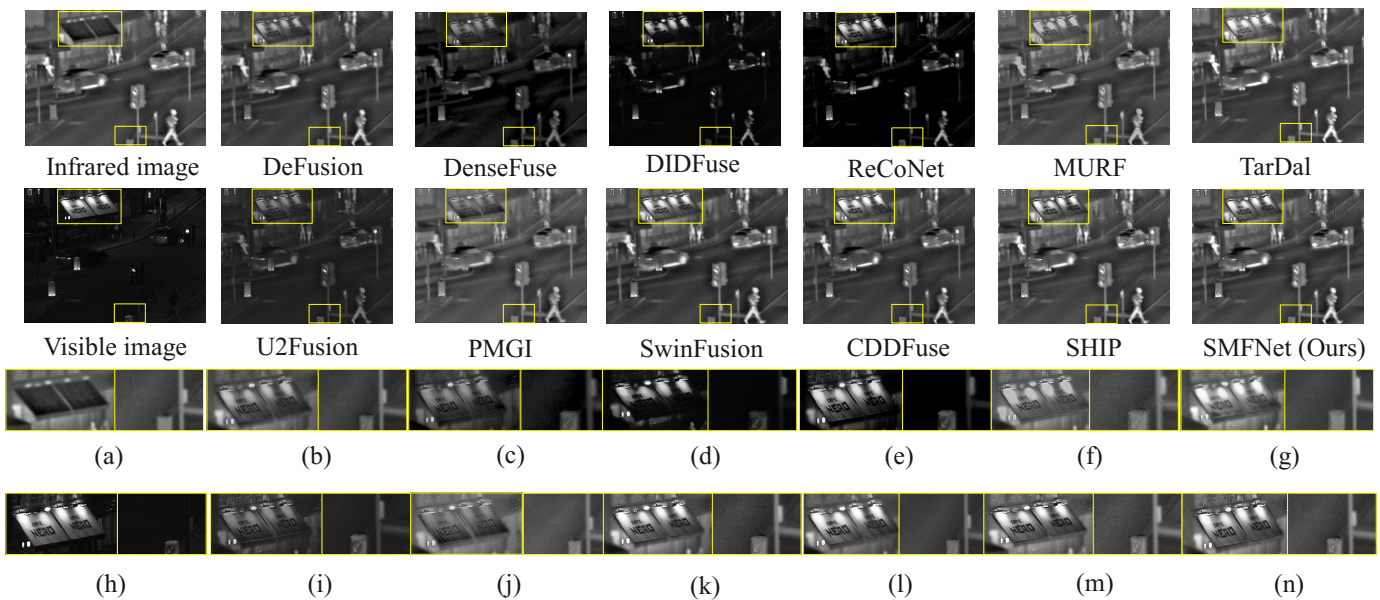
Fig. 5. Qualitative fusion results on TNO [71] dataset. Magnified areas from (a) to (n) show the performance of the shade board on the eave and the traffic sign arrow pointing downwards to the left, corresponding to the visible, infrared, and fused images generated by the state-of-the-art methods.
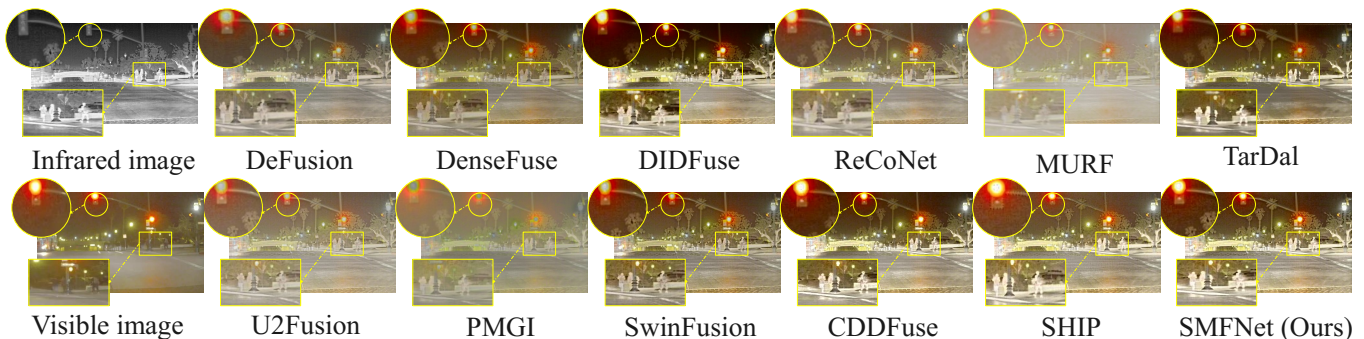

Fig. 6. Qualitative fusion results on RoadScene [16] dataset.

B. Comparision Settings

Eight evaluation metrics were employed to objectively measure the quality of fused images, including Entropy (EN), standard deviation (SD), spatial frequency (SF), mutual information (MI), sum of correlations of differences (SCD), visual information fidelity (VIF), Qabf, average gradient (AG), and structural similarity (SSIM). The larger values of the above metrics mean better image quality. Detailed descriptions of these metrics can be referenced in [26], [72]. We compared the proposed model with eleven state-of-the-art methods: DeFusion [36], DenseFuse [21], DIDFuse [25], MURF [41], ReCoNet [37], SwinFusion [19], TarDAL [4], U2Fusion [16], PMGI [18], CDDFuse [26] and SHIP [42]. We directly run the vanilla codes released by the authors on the three test datasets.

C. Infrared-Visible Fusion Results (RQ1)

1) Qualitative comparison: In this section, we show qualitative results on TNO [71], Roadscene [16] and MSRS [70] datasets in Fig. 5, 6 and 7, respectively. Through thorough observation and comparison, our method embodies satisfactory

visual performance compared with other SOTA methods. For example, targets in dark environments can be highlighted, such as people and cars. Furthermore, a clear background in the visible scene allows for the display of rich texture details. Notably, with attention to lighting, we can discern clear shape and contour information.

2) Quantitative comparison: In Tab. I, we present eight evaluation metrics across three test sets for quantitative analysis. Specifically, the highest EN and AG indicate significant preservation of information from the source images in our fused images, thanks to the cross-attention invertible module and effective complementary feature aggregation. The attention to targeted edge contours is largely attributed to the semantic loss function. Additionally, the highest values of VIF and Qabf indicate that the generated fused images exhibit excellent visual performance suitable for the human visual system and are also well-suited for subsequent computer vision tasks. Furthermore, the highest SF demonstrates good texture details in our results.
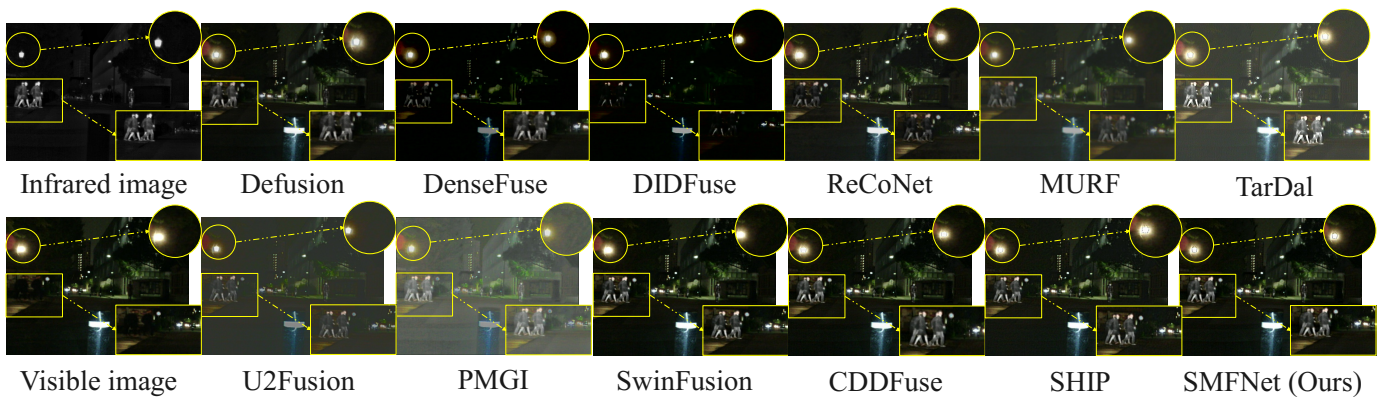
Fig. 7. Qualitative fusion results on MSRS [70] dataset.

TABLE I
QUANTITATIVE EVALUATION RESULTS OF IVF TASK, WHERE RED INDICATES THE BEST RESULTS, AND BLUE SHOWS THE SECOND-BEST VALUES.

Method	TNO Infrared-Visible Fusion Dataset							RoadScene Infrared-Visible Fusion Dataset							MSRS Infrared-Visible Fusion Dataset						
	EN	SD	SF	MI	VIF	Qabf	AG	SSIM	EN	SD	SF	MI	VIF	Qabf	AG	SSIM	EN	SD	SF	MI	VIF	Qabf	AG	SSIM
DeFusion [36]	6.5822	30.9861	6.5973	1.7573	0.5528	0.3589	3.7822	1.4246	6.8545	34.4052	7.7822	2.1668	0.5746	0.4129	4.3117	1.4486	6.3825	35.4282	8.1468	2.0686	0.7304	0.5067	3.7396	1.4400
DenseFuse [21]	6.2963	27.1425	7.0023	1.4947	0.5519	0.3394	3.7325	1.3891	6.6234	28.5042	7.4016	1.985	0.562	0.3688	3.9822	1.4716	4.7287	26.2808	6.3539	1.4026	0.4298	0.2899	2.6237	0.8176
DIDFuse [25]	6.8621	46.8716	11.7683	1.6953	0.593	0.4033	6.0095	1.1797	7.3207	52.8861	13.6309	2.0969	0.6215	0.4855	7.3586	1.2839	4.5002	29.6771	9.6158	1.4373	0.3054	0.2038	2.9108	0.8365
ReCoNet [37]	6.6775	40.4573	7.958	1.7181	0.5307	0.3728	4.7424	1.2751	7.1903	46.5624	9.753	2.1219	0.5491	0.3848	5.5852	1.3351	6.501	40.0413	9.0682	2.1484	0.6927	0.4913	4.5338	1.3155
MURF [41]	6.5402	30.7797	12.2408	1.6282	0.5566	0.4286	6.3707	1.3367	6.1869	21.6954	7.1072	1.4761	0.2033	0.1562	3.6145	1.1126	6.1556	28.5848	4.7218	1.6651	0.4269	0.1583	2.4601	1.0879
TarDal [4]	6.7795	40.6012	11.4994	1.9477	0.5677	0.4113	5.8702	1.3149	7.0848	42.7459	11.1432	2.4321	0.5826	0.4386	5.7274	1.3677	6.3476	35.4603	9.8727	1.8341	0.6728	0.4255	3.3889	1.0186
U2Fusion [16]	6.4175	26.337	8.8514	1.3468	0.5391	0.4251	5.0897	1.4120	6.7108	29.507	10.2725	1.8396	0.5599	0.4914	5.7803	1.4350	4.9532	18.869	6.7124	1.3533	0.4742	0.315	2.9513	1.0379
PMGI [18]	6.9519	35.832	8.9051	1.6512	0.6034	0.4119	5.0468	1.3509	6.7964	31.9394	7.5574	2.0768	0.5442	0.3591	4.333	1.3611	5.8333	18.1081	6.0163	1.3504	0.6175	0.2731	3.0761	0.8686
SwinFusion [19]	6.8998	41.1725	11.372	2.3132	0.7572	0.5381	6.1813	1.3771	6.8274	31.7477	12.8767	1.7429	0.6093	0.584	6.8742	1.4344	6.6185	42.9849	11.0554	3.3303	1.0056	0.6693	4.9865	1.4201
CDDFuse [26]	7.1203	46.001	13.1515	2.1861	0.7682	0.5393	6.9245	1.3411	7.4366	54.669	16.3633	2.2996	0.6948	0.5242	8.2131	1.3536	6.7012	43.3844	11.5566	3.4715	1.0509	0.6929	5.2811	1.3931
SHIP [42]	6.9475	40.7861	12.9417	2.8147	0.7752	0.5787	6.8979	1.3114	7.1546	44.672	14.5852	2.8331	0.7072	0.5763	7.7069	1.3425	6.4307	41.1334	11.8149	2.861	0.9075	0.6582	5.5415	1.3101
SMFNet (Ours)	7.1106	43.9525	13.6222	2.1574	0.7846	0.584	7.2613	1.3233	7.3909	51.7062	16.4399	2.3024	0.7328	0.5831	8.6128	1.3300	6.7021	42.9562	11.6976	3.1131	1.0448	0.7097	5.4765	1.3905

D. Infrared-Visible Object Detection (RQ2)

1) Setup: To rigorously compare the efficacy of fusion algorithms on object detection tasks, the data set and the detection method are fixed. The M^3FD dataset [4] is utilized to assess the impact of the proposed fusion model on object detection tasks. This dataset comprises 4200 pairs of infrared and visible images, which are divided into training, validation, and testing sets at a ratio of 8:1:1, respectively. The dataset encompasses six categories: people, cars, buses, motorbikes, trucks, and lamps. YOLOV5x[1] is employed as the object detector. The training process spans 100 epochs, with a batch size of 8 and the SGD optimizer set with an initial learning rate of $1e^{-2}$. The primary evaluation metric employed is the Mean Average Precision (MAP) at an Intersection over Union (IoU) threshold of 0.5 (MAP@0.5). This metric quantifies the model's ability to detect objects within images accurately.

2) Compared with SOTA methods: Tab. II and Fig. 8 display quantitative and qualitative results concerning object detection on M^3FD dataset. SHIP [42] has the best detection performance on the truck. ReCoNet [37], SwinFusion [19] and CDDFuse [26] also show their strengths in detecting major objects in real street scenes, especially for the cars and buses. Benefiting from the robust multi-guided architecture, the proposed model has the best detection performance in five classes, which demonstrates that generated fused images with specific characteristics can not only highlight targets difficult to detect but also preserve fundamental texture information.

TABLE II
DETECTION COMPARISONS OF OUR METHOD WITH ELEVEN STATE-OF-THE-ART METHODS ON M^3FD [4] DATASET. RED INDICATES THE BEST RESULTS, AND BLUE SHOWS THE SECOND-BEST VALUES.

Method	AP@0.5						mAP@0.5
	People	Car	Bus	Lamp	Motor	Truck	
DeFusion [36]	0.644	0.888	0.823	0.799	0.628	0.796	0.763
DenseFuse [21]	0.696	0.911	0.847	0.856	0.627	0.828	0.794
DIDFuse [25]	0.649	0.911	0.832	0.846	0.678	0.829	0.791
ReCoNet [37]	0.697	0.914	0.855	0.886	0.7	0.842	0.816
MURF [41]	0.641	0.872	0.806	0.809	0.645	0.759	0.755
TarDal [4]	0.647	0.878	0.82	0.779	0.639	0.844	0.768
U2Fusion [16]	0.499	0.681	0.482	0.136	0.318	0.498	0.436
PMGI [18]	0.606	0.866	0.786	0.735	0.484	0.751	0.705
SwinFusion [19]	0.69	0.919	0.85	0.868	0.683	0.83	0.807
CDDFuse [26]	0.714	0.919	0.86	0.877	0.71	0.835	0.819
SHIP [42]	0.683	0.914	0.859	0.883	0.727	0.862	0.821
SMFNet	0.723	0.925	0.862	0.903	0.738	0.856	0.835

E. Infrared-Visible Segmentation (RQ2)

1) Setup: DeepLabv3+ [73] is employed as the backbone to conduct semantic segmentation. MFNet dataset [74] is divided into training and test sets following the settings in [6]. The model is supervised by cross-entropy loss with SGD optimizer and initial learning rate of $1e^{-2}$. There are totally 300 epochs. The mean accuracy (mACC) and mean intersection-over-union (mIoU) are employed as the evaluation metrics for segmentation quality.

2) Compared with SOTA methods: The quantitative evaluation is shown in Tab. III. TarDal [4], SwinFusion [19] and CDDFuse [26] enable to efficiently classify unlabelled pixel regions. Besides, PMGI [18] has the highest segmentation accuracy. SwinFusion [19] and CDDFuse [26] have the highest value of mIoU on recognizing the car and person classes. Our proposed model has shown competitive results, especially in

---

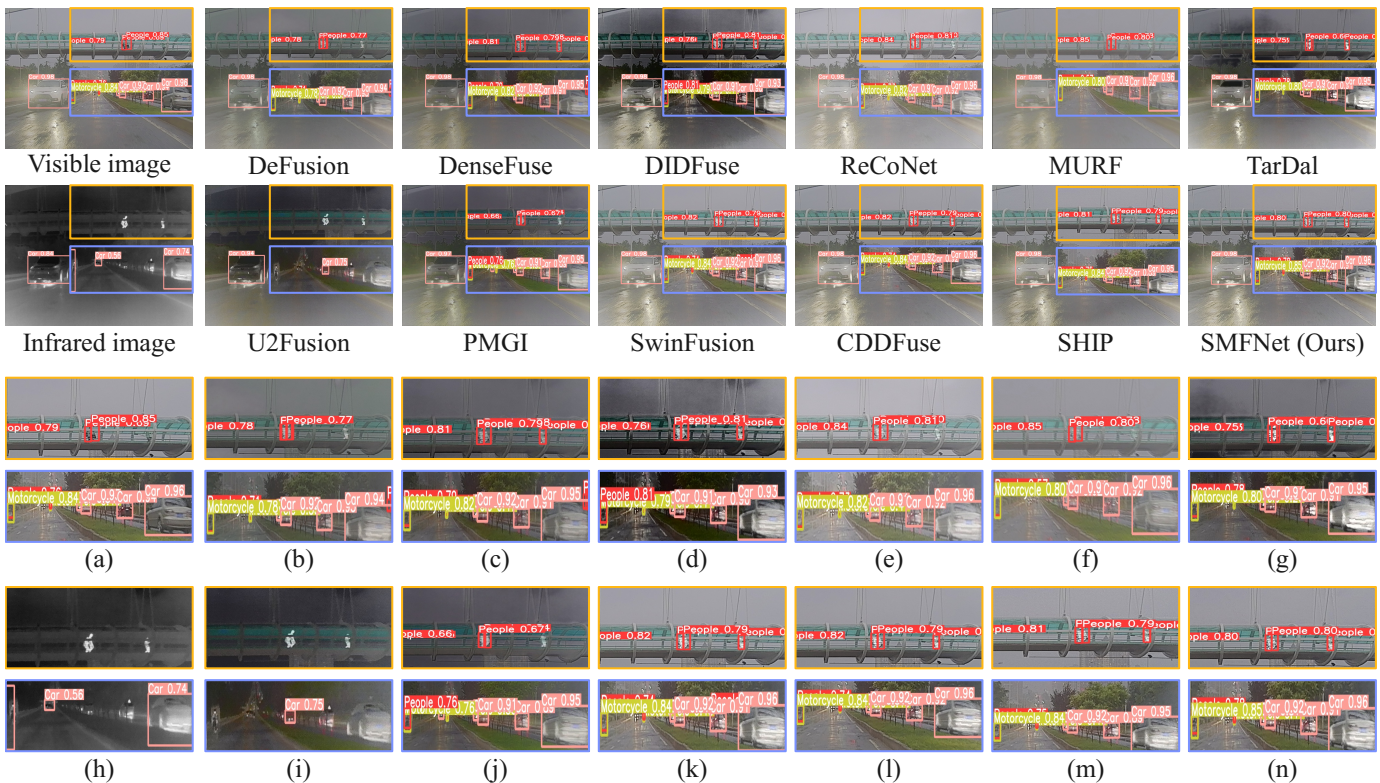[1] YOLOV5: https://github.com/ultralytics/yolov5

Fig. 8. Qualitative detection results on M^3FD dataset [4]. Magnified areas from (a) to (n) show the detection results of people walking on the pedestrian bridge, the motorbike and cars on the road, corresponding to the visible, infrared, and fused images generated by the state-of-the-art methods.

TABLE III
SEGMENTATION COMPARISONS OF OUR METHOD WITH NINE STATE-OF-THE-ART METHODS ON $MFNet$ [74] DATASET. **RED** INDICATES THE BEST RESULTS, AND **BLUE** SHOWS THE SECOND-BEST VALUES.

| Method | IoU | | | | | | | | mAcc | mIoU |
	Unlabel	Car	Person	Bike	Curve	Stop	Cone	Bump		
DeFusion	0.962	0.673	0.415	0.387	0.157	0.100	0.199	0.113	0.624	0.339
DenseFuse	0.961	0.658	0.390	0.480	0.154	0.118	0.298	0.267	0.610	0.376
DIDFuse	0.961	0.649	**0.439**	0.429	0.084	0.100	0.287	0.206	0.587	0.356
ReCoNet	0.963	0.693	0.410	**0.493**	**0.167**	0.110	0.310	0.065	0.581	0.360
MURF	0.957	0.592	0.285	0.379	0.054	0.086	0.284	0.008	0.567	0.294
TarDal	**0.964**	0.697	0.414	0.448	0.102	0.091	0.267	0.093	0.628	0.347
U2Fusion	0.944	0.317	0.348	0.048	0.005	0.023	0.116	0.122	0.569	0.214
PMGI	0.957	0.573	0.296	0.294	0.061	**0.124**	0.201	0.229	**0.646**	0.312
SwinFusion	**0.965**	**0.703**	**0.440**	0.483	**0.167**	**0.135**	**0.315**	**0.280**	0.637	**0.394**
CDDFuse	**0.965**	**0.702**	**0.440**	0.449	0.157	0.119	0.307	**0.338**	0.629	0.390
SHIP	0.960	0.621	0.342	0.447	0.130	0.094	0.303	0.154	0.628	0.342
SMFNet	**0.965**	0.700	0.427	**0.499**	**0.187**	0.122	**0.328**	0.268	**0.640**	**0.397**

the bike and cone regions. By observing Fig. 9, Some methods, for example, DIDFuse [25], MURF [41], TarDal [4], U2Fusion [16] and PMGI [18] have difficulties in distinguishing the curves and SHIP [42] is hard to recognize car stops. SMFNet can better integrate the edge and contour information, and consequently makes semantic segmentation more accurate.

*F. Extension to Medical Image Fusion (**RQ3**)*

As an extension task to validate the generalizability of our methodology, we construct a dataset sourced from the

Harvard Medical Website[2], including MRI-CT, MRI-PET and MRI-SPECT as training sets for the medical image fusion (MIF) task. There are 41 pairs of MRI-PET as testing sets. Since the hyperparameters are configured identically to those of the VIF task, there is no need for a validation set. The compared methods are CSMCA [75], NSST-PAPCNN [76], MATR [77], GeSeNet [78], MsgFusion [79], EMFusion [80] and IFCNN [17]. The fused medical images and objective evaluation results are listed in Fig. 10 and Tab. IV. The fused medical images compared in Fig. 10 demonstrate the
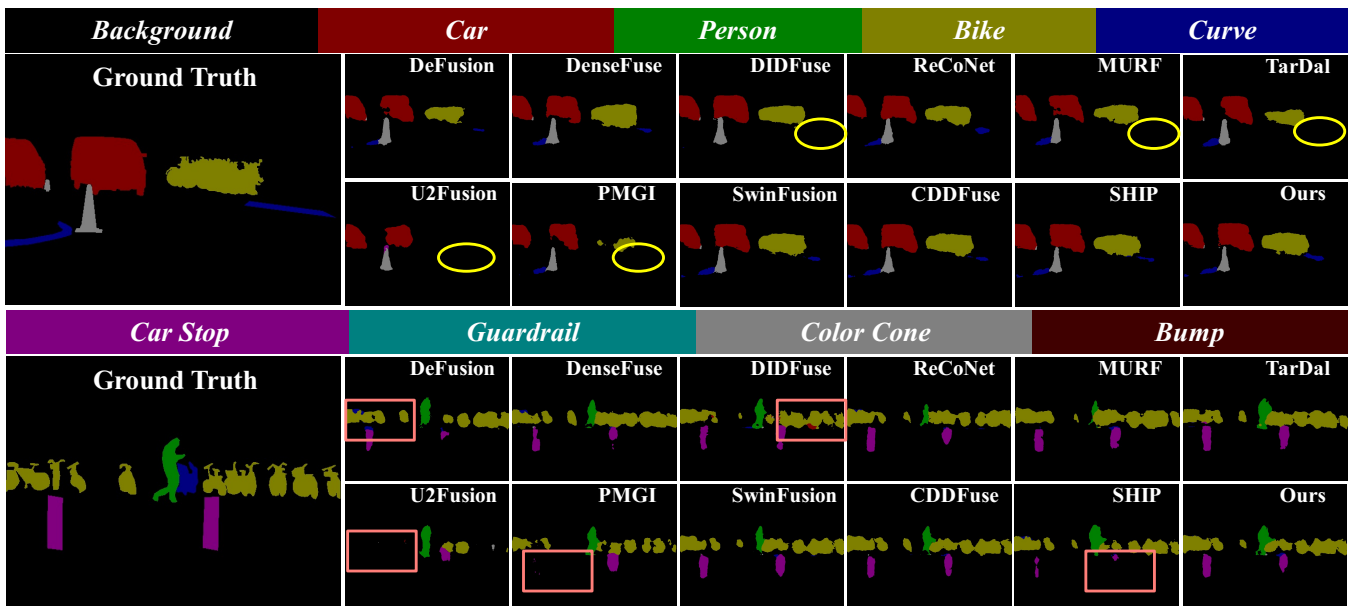
---

[2]http://www.med.harvard.edu/AANLIB/home.html

Fig. 9. Visual comparison of semantic segmentation about fused images from nine fusion methods on the $MFNet$ [74] dataset. The yellow and pink regions show missing and error segmentation, respectively.
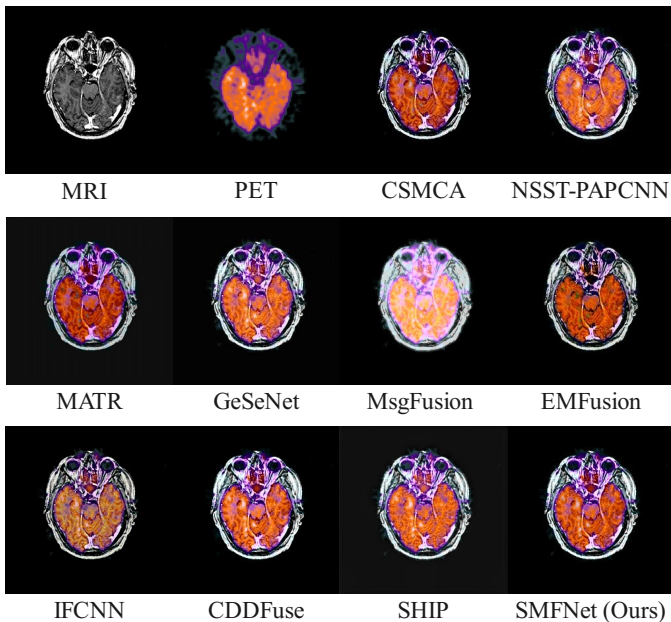

Fig. 10. Fused images from the above eight fusion methods on MIF dataset. CSMCA [75] and NSST-PAPCNN [76] are traditional algorithms, others are based on deep learning networks. SHIP [42] is the result obtained without using the medical image dataset for training. Experiments show that our method retains soft tissue imaging features and contains rich color expressions.

superiority of the proposed model in perserving the structural information from MRI and the pseudo-color from PET. The objective evaluation results in Tab. IV further confirm that the proposed model can generate satisfactory fused images.

G. Ablation Study ($\mathbf{RQ4}$, $\mathbf{RQ5}$ and $\mathbf{RQ6}$)

In this subsection, we mainly validate the effectiveness of each module, feature decomposition and aggregation, and the

TABLE IV
EXTENSIVE MRI-PET FUSION EXPERIMENT ON HARVARD MEDICAL DATASET. † REPRESENTS THE RESULTS AFTER TRAINING ON MIF DATASETS. **RED** INDICATES THE BEST RESULTS, AND **BLUE** SHOWS THE SECOND-BEST VALUES.

Method	Medical Image Fusion Dataset					
	MI	SF	VIF	Qabf	AG	SSIM
U2Fusion [16]	1.3879	12.2345	0.364	0.1933	3.8837	0.2086
TarDAL [4]	1.6094	18.1134	0.4268	0.3641	5.0768	0.2124
ReCoNet [37]	1.4408	11.1291	0.3717	0.1777	4.5917	0.2236
DeFusion [36]	1.5514	20.322	0.4439	0.4537	5.8414	1.5674
CDDFuse [26]	1.6226	28.5224	0.506	0.606	7.7348	1.7153
SHIP [42]	1.5968	28.0829	0.4754	0.632	8.5999	0.3374
SMFNet (Ours)	1.7284	32.6262	0.5881	0.7179	9.2834	0.3267
CSMCA† [75]	1.603	33.9865	0.5604	0.6939	8.95	1.5506
NSST-PAPCNN† [76]	1.6361	31.4735	0.5407	0.6594	8.6443	1.4757
MATR† [77]	1.7516	25.6819	0.689	0.7202	7.3149	0.2793
GeSeNet† [78]	1.6475	30.5983	0.5187	0.6844	8.8408	0.3049
MsgFusion† [79]	1.6138	21.5543	0.3802	0.3814	6.0622	1.4825
EMFusion† [80]	1.644	30.4133	0.559	0.6879	8.4637	1.5531
IFCNN† [17]	1.5663	32.7834	0.5292	0.6874	8.9715	1.6058
CDDFuse† [26]	1.7681	34.9976	0.6638	0.7327	9.674	1.7132
SMFNet (Ours)†	1.8031	32.3699	0.6739	0.7366	9.0584	1.6155

reason for the two training stages. EN, SD, VIF and SSIM are employed as the objective metrics. Experiment results are shown in Tab. VI.

1) Analysis on Modules: To validate the proposed CAI's effectiveness, we replace it with the basic INN block (ID=AE1 in Tab. VI). The performance deteriorated as there was no cross-attention mechanism to enhance local semantic features. Note, different from the typical paradigm using cross attention to achieve cross-modal interaction, CAI is an implicit way to enhance high-frequency information. Additionally, we employed 4 stacked transformer blocks shown in Fig. 2 (d) without residual connections to capture low-frequency information in the encoder branch (ID=AE2). The results show that combining residual connections with CNNs improves long-

TABLE V
MODEL COMPLEXITY AND RUNNING TIME ON $MSRS$ DATASET.

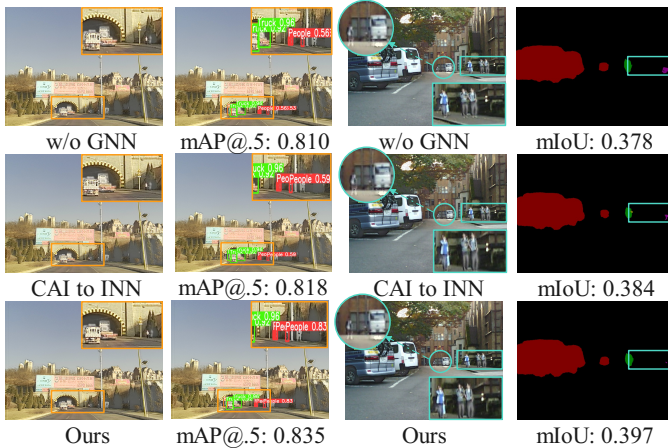| Metrics	DeFusion	DenseFuse	DIDFuse	ReCoNet	MURF	TarDal	U2Fusion	PMGI	SwinFusion	CDDFuse	SHIP	SMFNet
Flops (G)	81	27	115	7	185	91	**1e-3**	**1e-6**	308	548	157	1462
Params (K)	8043	74	373	**8**	116	297	659	**42**	927	1783	526	4504
Time (s)	0.05	**0.01**	**0.01**	0.03	0.7	**0.02**	0.64	0.1	1.04	0.16	0.1	0.32

Fig. 11. Ablation results of modules detection and segmentation on two datasets, M^3FD (left) and $MFNet$ (right). The values of mIoU and mAP@.5 are listed as well.

TABLE VI
ABLATION EXPERIMENT RESULTS IN THE TEST SET OF ROADSCENE [16]. **RED** INDICATES THE BEST RESULTS, AND **BLUE** SHOWS THE SECOND-BEST VALUES.

ID	Configurations	EN	SD	VIF	SSIM
AE1	from CAI to INN block	7.3257	49.5447	0.7139	0.9417
AE2	BFE w/o residual connections	7.3592	50.4884	0.7056	0.9291
AE3	w/o GNN	7.3692	50.9436	0.7027	0.9102
AE4	exchange detail and base fusion layer	7.3584	50.8266	0.7247	**0.9482**
AE5	w/o $\mathcal{L}_{semantic}^{I}$	7.3579	50.7396	**0.7297**	0.9401
AE6	two-stage both with $CC(\Phi_G^V, \Phi_G^I)$	**7.3765**	**51.4596**	0.7248	0.9333
AE7	w/o two-stage training	7.365	50.4629	0.6906	0.9237
AE8	SMFNet	**7.3909**	**51.7062**	**0.7328**	**0.9554**

range expression abilities. SMFNet without GNN (ID=AE3) leads to inadequate detailed feature extraction, which also affects performance across downstream tasks, as shown in Fig. 11. Lastly, in order to verify the proper fusion rules, we swapped two fusion layers (ID=AE4) to determine their optimal positions for the fusion stage.

2) Features Decomposition and Aggregation: In this part, we discuss the proposed semantic loss in training stage I (ID=AE5) and the correlation-driven GNN loss proposed in training stage II (ID=AE6). During the experiment, we found that two training stages both with the guidance of correlation loss function, made the fused images reduce information preservation and have low contrast. We hypothesize that GNN does not need explicit correlation restriction when executing the image reconstruction task. And in the fusion stage, it's necessary to increase correlations between nodes **C** and **D** (explained in Sec. III-B4) as detail features. Gram matrix brings salient targets and maintains many texture details. $CC(\Phi_G^V, \Phi_G^I)$ in the second stage further enhances cross-

modality interaction and balance between high-frequency and low-frequency information.

3) Two Training Stages: To validate the importance of two training stages, we directly train the encoder, decoder and fusion layers together (ID=AE7) with 120 epochs. The results are unsatisfactory. Pre-trained encoder and decoder show more powerful feature extraction abilities and promote training in the second stage to generate better performance on qualitative and quantitative results.

H. Efficiency Comparison

Tab. V lists the computational costs and execution time of the twelve image fusion methods on the 361 image pairs of the MSRS test set with the size of 640×480. MURF, U2Fusion and PMGI run on TensorFlow platform with CPU. Other methods run on Pytorch with GPU acceleration. By numerical comparison, U2Fusion and PMGI have the minimal computational load. Additionally, The model of ReCoNet only has 8K parameters. DenseFuse and DIDFuse spend an average of 0.01 seconds generating per fused image. The proposed SMFNet spends less generating time than SwinFusion and has fewer parameters than DeFusion.

V. CONCLUSION

In this paper, a semantic-aware multi-guided network for infrared-visible image fusion was proposed. Graph Reasoning module models and reasons about high-level relations between two modalities and extract low-level detail features. Cross Attention and Invertible Block (CAI) solves information loss during the decomposing process to extract high-frequency features. Additionally, a base feature extraction module equipped with Multi-Dconv Head Transposed Attention (MDTA) and Local-enhanced Feed Forward (LeFF) network is primarily utilized to capture global features with long-range dependencies. Two novel loss functions are proposed as the restriction in two training stages. Experiments demonstrate the fusion effect of our proposed SMFNet and the accuracy of downstream pattern recognition tasks can also be improved. In further works, we will explore multi-task learning (MTL) including image reconstruction, fusion tasks and scene parsing, considering novel joint-optimization among these tasks soon.

REFERENCES

[1] L. Tang, Z. Chen, J. Huang, and J. Ma, "Camf: An interpretable infrared and visible image fusion network based on class activation mapping," *IEEE Transactions on Multimedia*, vol. 26, pp. 4776–4791, 2024.

[2] W. Tang, F. He, and Y. Liu, "Ydtr: Infrared and visible image fusion via y-shape dynamic transformer," *IEEE Transactions on Multimedia*, vol. 25, pp. 5413–5428, 2023.

[3] R. Nie, C. Ma, J. Cao, H. Ding, and D. Zhou, "A total variation with joint norms for infrared and visible image fusion," *IEEE Transactions on Multimedia*, vol. 24, pp. 1460–1472, 2022.

[4] J. Liu, X. Fan, Z. Huang, G. Wu, R. Liu, W. Zhong, and Z. Luo, "Target-aware dual adversarial learning and a multi-scenario multi-modality benchmark to fuse infrared and visible for object detection," in *Proceedings of the IEEE/CVF Conference on Computer Vision and Pattern Recognition*, 2022, pp. 5802–5811.

[5] E. Xie, W. Wang, Z. Yu, A. Anandkumar, J. M. Alvarez, and P. Luo, "Segformer: Simple and efficient design for semantic segmentation with transformers," *Advances in Neural Information Processing Systems*, vol. 34, pp. 12 077–12 090, 2021.

[6] J. Liu, Z. Liu, G. Wu, L. Ma, R. Liu, W. Zhong, Z. Luo, and X. Fan, "Multi-interactive feature learning and a full-time multi-modality benchmark for image fusion and segmentation," in *Proceedings of the IEEE/CVF International Conference on Computer Vision*, 2023, pp. 8115–8124.

[7] H. Zhang, X. Zuo, H. Zhou, T. Lu, and J. Ma, "A robust mutual-reinforcing framework for 3d multi-modal medical image fusion based on visual-semantic consistency," in *Proceedings of the AAAI Conference on Artificial Intelligence*, vol. 38, no. 7, 2024, pp. 7087–7095.

[8] F. Yang, X. Li, H. Duan, F. Xu, Y. Huang, X. Zhang, Y. Long, and Y. Zheng, "Mrl-seg: Overcoming imbalance in medical image segmentation with multi-step reinforcement learning," *IEEE Journal of Biomedical and Health Informatics*, vol. 28, no. 2, pp. 858–869, 2024.

[9] R. Wang, X. Li, M. Tian, F. Yang, and X. Zhang, "Patch-level knowledge distillation and regularization for missing modality medical image segmentation," in *ICASSP 2024-2024 IEEE International Conference on Acoustics, Speech and Signal Processing (ICASSP)*. IEEE, 2024, pp. 2240–2244.

[10] W. G. C. Bandara and V. M. Patel, "Hypertransformer: A textural and spectral feature fusion transformer for pansharpening," in *Proceedings of the IEEE/CVF Conference on Computer Vision and Pattern Recognition*, 2022, pp. 1767–1777.

[11] J. Ma, H. Xu, J. Jiang, X. Mei, and X.-P. Zhang, "Ddcgan: A dual-discriminator conditional generative adversarial network for multi-resolution image fusion," *IEEE Transactions on Image Processing*, vol. 29, pp. 4980–4995, 2020.

[12] J. Ma, W. Yu, P. Liang, C. Li, and J. Jiang, "Fusiongan: A generative adversarial network for infrared and visible image fusion," *Information fusion*, vol. 48, pp. 11–26, 2019.

[13] H. Xu, J. Ma, and X.-P. Zhang, "Mef-gan: Multi-exposure image fusion via generative adversarial networks," *IEEE Transactions on Image Processing*, vol. 29, pp. 7203–7216, 2020.

[14] J. Ma, H. Zhang, Z. Shao, P. Liang, and H. Xu, "Ganmcc: A generative adversarial network with multiclassification constraints for infrared and visible image fusion," *IEEE Transactions on Instrumentation and Measurement*, vol. 70, pp. 1–14, 2020.

[15] C. Zhao, P. Yang, F. Zhou, G. Yue, S. Wang, H. Wu, G. Chen, T. Wang, and B. Lei, "Mhw-gan: Multidiscriminator hierarchical wavelet generative adversarial network for multimodal image fusion," *IEEE Transactions on Neural Networks and Learning Systems*, pp. 1–15, 2023.

[16] H. Xu, J. Ma, J. Jiang, X. Guo, and H. Ling, "U2fusion: A unified unsupervised image fusion network," *IEEE Transactions on Pattern Analysis and Machine Intelligence*, vol. 44, no. 1, pp. 502–518, 2020.

[17] Y. Zhang, Y. Liu, P. Sun, H. Yan, X. Zhao, and L. Zhang, "Ifcnn: A general image fusion framework based on convolutional neural network," *Information Fusion*, vol. 54, pp. 99–118, 2020.

[18] H. Zhang, H. Xu, Y. Xiao, X. Guo, and J. Ma, "Rethinking the image fusion: A fast unified image fusion network based on proportional maintenance of gradient and intensity," in *Proceedings of the AAAI Conference on Artificial Intelligence*, vol. 34, no. 07, 2020, pp. 12 797–12 804.

[19] J. Ma, L. Tang, F. Fan, J. Huang, X. Mei, and Y. Ma, "Swinfusion: Cross-domain long-range learning for general image fusion via swin transformer," *IEEE/CAA Journal of Automatica Sinica*, vol. 9, no. 7, pp. 1200–1217, 2022.

[20] Y. Guan, R. Xu, M. Yao, L. Wang, and Z. Xiong, "Mutual-guided dynamic network for image fusion," in *Proceedings of the 31st ACM International Conference on Multimedia*, 2023, pp. 1779–1788.

[21] H. Li and X.-J. Wu, "Densefuse: A fusion approach to infrared and visible images," *IEEE Transactions on Image Processing*, vol. 28, no. 5, pp. 2614–2623, 2018.

[22] H. Li, X.-J. Wu, and T. Durrani, "Nestfuse: An infrared and visible image fusion architecture based on nest connection and spatial/channel attention models," *IEEE Transactions on Instrumentation and Measurement*, vol. 69, no. 12, pp. 9645–9656, 2020.

[23] L. Jian, X. Yang, Z. Liu, G. Jeon, M. Gao, and D. Chisholm, "Sedrfuse: A symmetric encoder–decoder with residual block network for infrared and visible image fusion," *IEEE Transactions on Instrumentation and Measurement*, vol. 70, pp. 1–15, 2020.

[24] J. Liu, Y. Wu, Z. Huang, R. Liu, and X. Fan, "Smoa: Searching a modality-oriented architecture for infrared and visible image fusion," *IEEE Signal Processing Letters*, vol. 28, pp. 1818–1822, 2021.

[25] Z. Zhao, S. Xu, C. Zhang, J. Liu, P. Li, and J. Zhang, "Didfuse: Deep image decomposition for infrared and visible image fusion," *arXiv preprint arXiv:2003.09210*, 2020.

[26] Z. Zhao, H. Bai, J. Zhang, Y. Zhang, S. Xu, Z. Lin, R. Timofte, and L. Van Gool, "Cddfuse: Correlation-driven dual-branch feature decomposition for multi-modality image fusion," in *Proceedings of the IEEE/CVF Conference on Computer Vision and Pattern Recognition*, 2023, pp. 5906–5916.

[27] J. J. Lewis, R. J. O'Callaghan, S. G. Nikolov, D. R. Bull, and N. Canagarajah, "Pixel-and region-based image fusion with complex wavelets," *Information fusion*, vol. 8, no. 2, pp. 119–130, 2007.

[28] G. Bhatnagar, Q. M. J. Wu, and Z. Liu, "Directive contrast based multimodal medical image fusion in nsct domain," *IEEE Transactions on Multimedia*, vol. 15, no. 5, pp. 1014–1024, 2013.

[29] H. Li, X.-J. Wu, and J. Kittler, "Mdlatlrr: A novel decomposition method for infrared and visible image fusion," *IEEE Transactions on Image Processing*, vol. 29, pp. 4733–4746, 2020.

[30] J. Ma, Z. Zhou, B. Wang, and H. Zong, "Infrared and visible image fusion based on visual saliency map and weighted least square optimization," *Infrared Physics & Technology*, vol. 82, pp. 8–17, 2017.

[31] Y. Yang, Y. Zhang, S. Huang, Y. Zuo, and J. Sun, "Infrared and visible image fusion using visual saliency sparse representation and detail injection model," *IEEE Transactions on Instrumentation and Measurement*, vol. 70, pp. 1–15, 2020.

[32] Z. Zhao, S. Xu, C. Zhang, J. Liu, and J. Zhang, "Bayesian fusion for infrared and visible images," *Signal Processing*, vol. 177, p. 107734, 2020.

[33] Z. Zhao, H. Bai, Y. Zhu, J. Zhang, S. Xu, Y. Zhang, K. Zhang, D. Meng, R. Timofte, and L. Van Gool, "Ddfm: denoising diffusion model for multi-modality image fusion," in *Proceedings of the IEEE/CVF International Conference on Computer Vision*, 2023, pp. 8082–8093.

[34] X. Wang, Y. Lin, Y. Shen, and P. Niu, "Udtcwt-phfms domain statistical image watermarking using vector bw-type r distribution," *IEEE Transactions on Circuits and Systems for Video Technology*, vol. 33, no. 10, pp. 5345–5359, 2023.

[35] G. Alain and Y. Bengio, "What regularized auto-encoders learn from the data-generating distribution," *The Journal of Machine Learning Research*, vol. 15, no. 1, pp. 3563–3593, 2014.

[36] P. Liang, J. Jiang, X. Liu, and J. Ma, "Fusion from decomposition: A self-supervised decomposition approach for image fusion," in *European Conference on Computer Vision*. Springer, 2022, pp. 719–735.

[37] Z. Huang, J. Liu, X. Fan, R. Liu, W. Zhong, and Z. Luo, "Reconet: Recurrent correction network for fast and efficient multi-modality image fusion," in *European Conference on Computer Vision*. Springer, 2022, pp. 539–555.

[38] R. Liu and Z. Lin, "Bilevel optimization for automated machine learning: a new perspective on framework and algorithm," *National Science Review*, vol. 11, no. 8, p. nwad292, 11 2023.

[39] H. Liu, K. Simonyan, and Y. Yang, "Darts: Differentiable architecture search," *arXiv preprint arXiv:1806.09055*, 2018.

[40] W. Zhao, S. Xie, F. Zhao, Y. He, and H. Lu, "Metafusion: Infrared and visible image fusion via meta-feature embedding from object detection," in *Proceedings of the IEEE/CVF Conference on Computer Vision and Pattern Recognition*, 2023, pp. 13 955–13 965.

[41] H. Xu, J. Yuan, and J. Ma, "Murf: Mutually reinforcing multi-modal image registration and fusion," *IEEE Transactions on Pattern Analysis and Machine Intelligence*, vol. 45, no. 10, pp. 12 148–12 166, 2023.

[42] N. Zheng, M. Zhou, J. Huang, J. Hou, H. Li, Y. Xu, and F. Zhao, "Probing synergistic high-order interaction in infrared and visible image fusion," in *Proceedings of the IEEE/CVF Conference on Computer Vision and Pattern Recognition*, 2024, pp. 26 384–26 395.

[43] A. Dosovitskiy, L. Beyer, A. Kolesnikov, D. Weissenborn, X. Zhai, T. Unterthiner, M. Dehghani, M. Minderer, G. Heigold, S. Gelly *et al.*, "An image is worth 16x16 words: Transformers for image recognition at scale," *arXiv preprint arXiv:2010.11929*, 2020.

[44] J. Liang, J. Cao, G. Sun, K. Zhang, L. Van Gool, and R. Timofte, "Swinir: Image restoration using swin transformer," in *Proceedings of the IEEE/CVF International Conference on Computer Vision*, 2021, pp. 1833–1844.

[45] Z. Wang, X. Cun, J. Bao, W. Zhou, J. Liu, and H. Li, "Uformer: A general u-shaped transformer for image restoration," in *Proceedings of the IEEE/CVF Conference on Computer Vision and Pattern Recognition*, 2022, pp. 17 683–17 693.

[46] J. Xiao, X. Fu, F. Wu, and Z.-J. Zha, "Stochastic window transformer for image restoration," *Advances in Neural Information Processing Systems*, vol. 35, pp. 9315–9329, 2022.

[47] A. Ali, H. Touvron, M. Caron, P. Bojanowski, M. Douze, A. Joulin, I. Laptev, N. Neverova, G. Synnaeve, J. Verbeek *et al.*, "Xcit: Cross-covariance image transformers," *Advances in Neural Information Processing Systems*, vol. 34, pp. 20 014–20 027, 2021.

[48] Z. Liu, H. Hu, Y. Lin, Z. Yao, Z. Xie, Y. Wei, J. Ning, Y. Cao, Z. Zhang, L. Dong *et al.*, "Swin transformer v2: Scaling up capacity and resolution," in *Proceedings of the IEEE/CVF Conference on Computer Vision and Pattern Recognition*, 2022, pp. 12 009–12 019.

[49] J. Xiao, X. Fu, A. Liu, F. Wu, and Z.-J. Zha, "Image de-raining transformer," *IEEE Transactions on Pattern Analysis and Machine Intelligence*, vol. 45, no. 11, pp. 12 978–12 995, 2023.

[50] D. Zhang, F. Huang, S. Liu, X. Wang, and Z. Jin, "Swinfir: Revisiting the swinir with fast fourier convolution and improved training for image super-resolution," *arXiv preprint arXiv:2208.11247*, 2022.

[51] S. W. Zamir, A. Arora, S. Khan, M. Hayat, F. S. Khan, and M.-H. Yang, "Restormer: Efficient transformer for high-resolution image restoration," in *Proceedings of the IEEE/CVF Conference on Computer Vision and Pattern Recognition*, 2022, pp. 5728–5739.

[52] J. Li, Y. Wang, and W. Li, "Mhrn: A multimodal hierarchical reasoning network for topic detection," *IEEE Transactions on Multimedia*, vol. 26, pp. 6968–6980, 2024.

[53] S. Wu, F. Sun, W. Zhang, X. Xie, and B. Cui, "Graph neural networks in recommender systems: a survey," *ACM Computing Surveys*, vol. 55, no. 5, pp. 1–37, 2022.

[54] T. N. Kipf and M. Welling, "Semi-supervised classification with graph convolutional networks," *arXiv preprint arXiv:1609.02907*, 2016.

[55] X. Wang and A. Gupta, "Videos as space-time region graphs," in *Proceedings of the European Conference on Computer Vision (ECCV)*, 2018, pp. 399–417.

[56] Y. Li and A. Gupta, "Beyond grids: Learning graph representations for visual recognition," *Advances in Neural Information Processing Systems*, vol. 31, 2018.

[57] K. Han, Y. Wang, J. Guo, Y. Tang, and E. Wu, "Vision gnn: An image is worth graph of nodes," *Advances in Neural Information Processing Systems*, vol. 35, pp. 8291–8303, 2022.

[58] Y. Han, P. Wang, S. Kundu, Y. Ding, and Z. Wang, "Vision hgnn: An image is more than a graph of nodes," in *Proceedings of the IEEE/CVF International Conference on Computer Vision*, 2023, pp. 19 878–19 888.

[59] C. Xu, Q. Li, X. Jiang, D. Yu, and Y. Zhou, "Dual-space graph-based interaction network for rgb-thermal semantic segmentation in electric power scene," *IEEE Transactions on Circuits and Systems for Video Technology*, vol. 33, no. 4, pp. 1577–1592, 2023.

[60] X. Hu, X. Zhang, F. Wang, J. Sun, and F. Sun, "Efficient camouflaged object detection network based on global localization perception and local guidance refinement," *IEEE Transactions on Circuits and Systems for Video Technology*, vol. 34, no. 7, pp. 5452–5465, 2024.

[61] X. Hu, F. Sun, J. Sun, F. Wang, and H. Li, "Cross-modal fusion and progressive decoding network for rgb-d salient object detection," *International Journal of Computer Vision*, pp. 1–19, 2024.

[62] A. Luo, X. Li, F. Yang, Z. Jiao, H. Cheng, and S. Lyu, "Cascade graph neural networks for rgb-d salient object detection," in *Computer Vision–ECCV 2020: 16th European Conference, Glasgow, UK, August 23–28, 2020, Proceedings, Part XII 16.* Springer, 2020, pp. 346–364.

[63] M. Zhou, K. Yan, J. Huang, Z. Yang, X. Fu, and F. Zhao, "Mutual information-driven pan-sharpening," in *Proceedings of the IEEE/CVF Conference on Computer Vision and Pattern Recognition*, 2022, pp. 1798–1808.

[64] J. Jing, X. Deng, M. Xu, J. Wang, and Z. Guan, "Hinet: deep image hiding by invertible network," in *Proceedings of the IEEE/CVF International Conference on Computer Vision*, 2021, pp. 4733–4742.

[65] Z. Guan, J. Jing, X. Deng, M. Xu, L. Jiang, Z. Zhang, and Y. Li, "Deepmih: Deep invertible network for multiple image hiding," *IEEE Transactions on Pattern Analysis and Machine Intelligence*, vol. 45, no. 1, pp. 372–390, 2022.

[66] M. Zhou, J. Huang, K. Yan, D. Hong, X. Jia, J. Chanussot, and C. Li, "A general spatial-frequency learning framework for multimodal image fusion," *IEEE Transactions on Pattern Analysis and Machine Intelligence*, pp. 1–18, 2024.

[67] Z. Wang, A. C. Bovik, H. R. Sheikh, and E. P. Simoncelli, "Image quality assessment: from error visibility to structural similarity," *IEEE Transactions on Image Processing*, vol. 13, no. 4, pp. 600–612, 2004.

[68] H. Li, T. Xu, X.-J. Wu, J. Lu, and J. Kittler, "Lrrnet: A novel representation learning guided fusion network for infrared and visible images," *IEEE Transactions on Pattern Analysis and Machine Intelligence*, vol. 45, no. 9, pp. 11 040–11 052, 2023.

[69] L. Tang, J. Yuan, and J. Ma, "Image fusion in the loop of high-level vision tasks: A semantic-aware real-time infrared and visible image fusion network," *Information Fusion*, vol. 82, pp. 28–42, 2022.

[70] L. Tang, J. Yuan, H. Zhang, X. Jiang, and J. Ma, "Piafusion: A progressive infrared and visible image fusion network based on illumination aware," *Information Fusion*, vol. 83, pp. 79–92, 2022.

[71] A. Toet and M. A. Hogervorst, "Progress in color night vision," *Optical Engineering*, vol. 51, no. 1, pp. 010 901–010 901, 2012.

[72] J. Ma, Y. Ma, and C. Li, "Infrared and visible image fusion methods and applications: A survey," *Information fusion*, vol. 45, pp. 153–178, 2019.

[73] L.-C. Chen, Y. Zhu, G. Papandreou, F. Schroff, and H. Adam, "Encoder-decoder with atrous separable convolution for semantic image segmentation," in *Proceedings of the European Conference on Computer Vision (ECCV)*, 2018, pp. 801–818.

[74] Q. Ha, K. Watanabe, T. Karasawa, Y. Ushiku, and T. Harada, "Mfnet: Towards real-time semantic segmentation for autonomous vehicles with multi-spectral scenes," in *2017 IEEE/RSJ International Conference on Intelligent Robots and Systems (IROS).* IEEE, 2017, pp. 5108–5115.

[75] Y. Liu, X. Chen, R. K. Ward, and Z. J. Wang, "Medical image fusion via convolutional sparsity based morphological component analysis," *IEEE Signal Processing Letters*, vol. 26, no. 3, pp. 485–489, 2019.

[76] M. Yin, X. Liu, Y. Liu, and X. Chen, "Medical image fusion with parameter-adaptive pulse coupled neural network in nonsubsampled shearlet transform domain," *IEEE Transactions on Instrumentation and Measurement*, vol. 68, no. 1, pp. 49–64, 2018.

[77] W. Tang, F. He, Y. Liu, and Y. Duan, "Matr: Multimodal medical image fusion via multiscale adaptive transformer," *IEEE Transactions on Image Processing*, vol. 31, pp. 5134–5149, 2022.

[78] J. Li, J. Liu, S. Zhou, Q. Zhang, and N. K. Kasabov, "Gesenet: A general semantic-guided network with couple mask ensemble for medical image fusion," *IEEE Transactions on Neural Networks and Learning Systems*, pp. 1–14, 2023.

[79] J. Wen, F. Qin, J. Du, M. Fang, X. Wei, C. P. Chen, and P. Li, "Msgfusion: Medical semantic guided two-branch network for multimodal brain image fusion," *IEEE Transactions on Multimedia*, vol. 26, pp. 944–957, 2023.

[80] H. Xu and J. Ma, "Emfusion: An unsupervised enhanced medical image fusion network," *Information Fusion*, vol. 76, pp. 177–186, 2021.